An interval of high salinity in ancient Gale crater lake on Mars

W. Rapin [1]*, B. L. Ehlmann[1,2], G. Dromart[3], J. Schieber[4], N. H. Thomas[1], W. W. Fischer[1], V. K. Fox[1], N. T. Stein[1], M. Nachon[5], B. C. Clark[6], L. C. Kah [7], L. Thompson[8], H. A. Meyer[1], T. S. J. Gabriel[9], C. Hardgrove[9], N. Mangold[10], F. Rivera-Hernandez [11], R. C. Wiens[12] and A. R. Vasavada[2]

Precipitated minerals, including salts, are primary tracers of atmospheric conditions and water chemistry in lake basins. Ongoing in situ exploration by the Curiosity rover of Hesperian (around 3.3–3.7 Gyr old) sedimentary rocks within Gale crater on Mars has revealed clay-bearing fluvio-lacustrine deposits with sporadic occurrences of sulfate minerals, primarily as late-stage diagenetic veins and concretions. Here we report bulk enrichments, disseminated in the bedrock, of 30–50 wt% calcium sulfate intermittently over about 150 m of stratigraphy, and of 26–36 wt% hydrated magnesium sulfate within a thinner section of strata. We use geochemical analysis, primarily from the ChemCam laser-induced breakdown spectrometer, combined with results from other rover instruments, to characterize the enrichments and their lithology. The deposits are consistent with early diagenetic, pre-compaction salt precipitation from brines concentrated by evaporation, including magnesium sulfate-rich brines from extreme evaporative concentration. This saline interval represents a substantial hydrological perturbation of the lake basin, which may reflect variations in Mars' obliquity and orbital parameters. Our findings support stepwise changes in Martian climate during the Hesperian, leading to more arid and sulfate-dominated environments as previously inferred from orbital observations.

Carbonate, chloride and sulfate salts provide geochemical fingerprints of the past chemistry of terrestrial lake basins. On Mars, such chemical sediments reflect systematic differences in dissolved ions that lead to distinctive chemical divides and mineral assemblages[1]. For example, in situ, widespread magnesium/calcium/iron sulfate enrichments within aeolian and interdune playa sediments at Meridiani Planum have been interpreted to have formed from acidic and saline early diagenetic brines[2]. Low-CO_3^{2-}, high-SO_4^{2-} and low-pH waters enriched in Fe(II) formed a unique assemblage of hydrated sulfate minerals, jarosite, silica and chloride minerals[3]. Under less acidic conditions, iron is relatively immobile, calcium/magnesium sulfate and chloride assemblages are favoured and carbonate minerals can form under sufficiently elevated CO_3^{2-} concentrations[1].

From orbit, a diversity of sulfate, carbonate and chloride salts is observed on Mars, reflecting fluid chemistries that vary both spatially and temporally[4]. Thick-layered sulfate deposits are observed at a number of late Noachian to late Hesperian locations (~3.5 billion years ago). Their apparent absence in the older stratigraphic record is hypothesized to reflect the diminishing availability of liquid water on Mars[5]. Gale crater provides an exemplary sedimentary succession dated to the Hesperian[6] that contains clay minerals transitioning to sulfate minerals over ~300 m of stratigraphy[7,8]. Understanding the reason for this transition is one of the primary objectives of the Mars Science Laboratory (MSL)/Curiosity rover investigation. To date, the rover has explored clay-bearing fluvio-lacustrine sedimentary record in the lowermost stratigraphy, which is dominated by

the formation of mineral assemblages that include authigenic or detrital clay minerals and iron oxides[9–12], with a potentially punctuated transition in redox state[10]. Sulfates have been observed mostly as abundant late-diagenetic calcium sulfate fracture-fills[13,14], and inferred from crystal pseudomorphs after gypsum, that occur locally in the lowermost Murray formation[15]. Magnesium was also observed, but was primarily associated with sparse diagenetic features such as concretions and dendrites[10,16,17].

Here we detail the chemistry of lacustrine deposits from the upper Murray formation heterolithic facies, which consists of interbedded sandstone and mudstone with exposures dominated by broken, tilted blocks with diverse resistance to erosion. This change in sedimentary facies in the Murray formation correlates with a gradual transition in the bedrock alteration index defined by major element compositions[18]. It also coincides with an increase in the prevalence of, chlorine and associated salts, which suggests the presence of distinctively saline waters.

Calcium sulfate bedrock enrichment

Starting at the base of the Sutton Island member (Fig. 1a), enrichment of calcium sulfate is observed within the bulk sedimentary bedrock, distinct from previous occurrences in fracture-fills and merely sporadic detections (targets with <50% of points enriched). Bulk enrichments are characterized by ChemCam analyses of bedrock, where the majority of sampled points exhibit compositions that correspond to binary mixtures of typical Murray bedrock (that is, average sulfate-free bedrock dominated by silicate minerals

[1]California Institute of Technology, Pasadena, CA, USA. [2]Jet Propulsion Laboratory, California Institute of Technology, Pasadena, CA, USA. [3]Laboratoire de Géologie de Lyon, Université de Lyon, Lyon, France. [4]Indiana University, Bloomington, IN, USA. [5]Texas A&M University, College Station, TX, USA. [6]Space Science Institute, Boulder, CO, USA. [7]University of Tennessee, Knoxville, TN, USA. [8]University of New Brunswick, Fredericton, Canada. [9]School of Earth and Space Exploration, Arizona State University, Tempe, AZ, USA. [10]Laboratoire de Planétologie et Géodynamique, UMR6112, CNRS, Université Nantes, Université Angers, Nantes, France. [11]Dartmouth College, Hanover, NH, USA. [12]Los Alamos National Laboratory, Los Alamos, NM, USA.
*e-mail: wrapin@caltech.edu
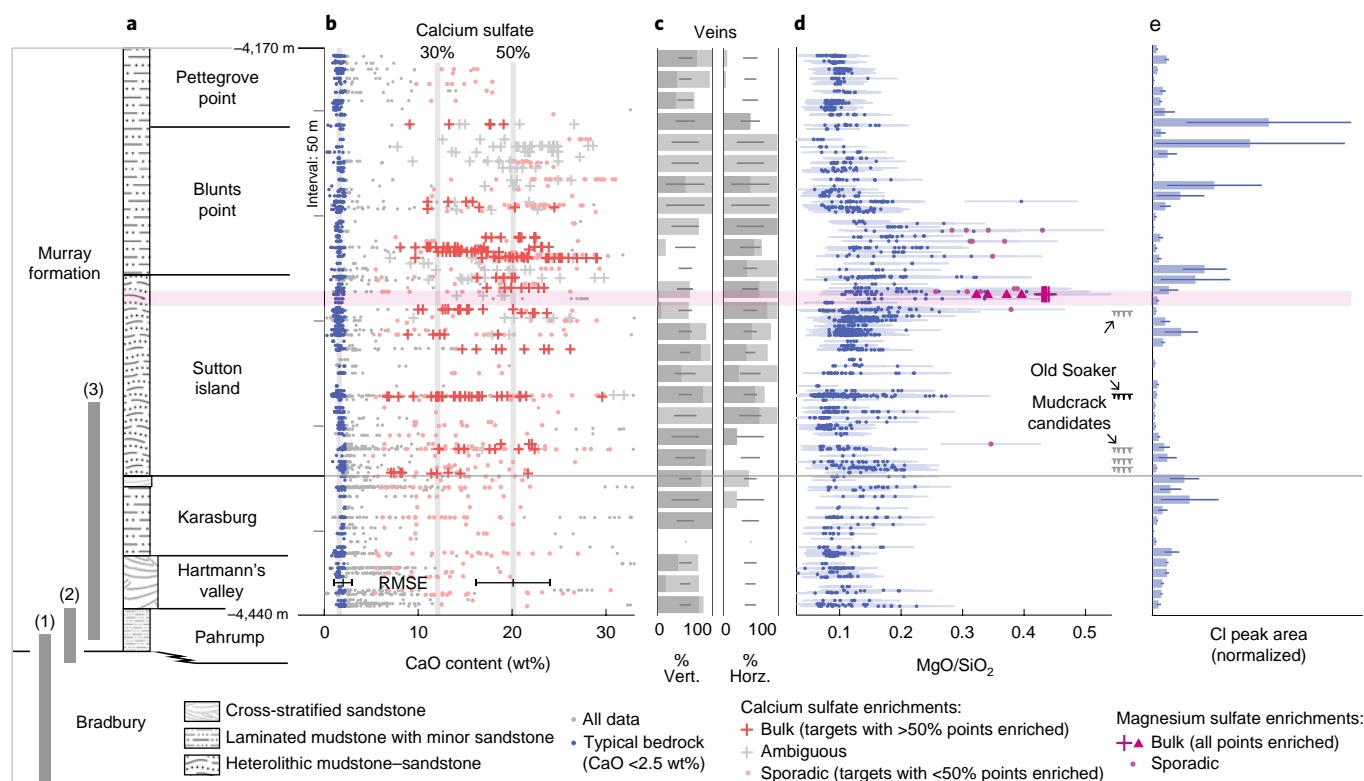
Fig. 1 | Stratigraphic context on bedrock composition. a, Overview of the ~350 m of stratigraphy explored in situ at Gale crater, including dominant facies observed[41] and sections highlighting evidence for: (1) fluvio-lacustrine environment[9], (2) lake redox stratification[10] and (3) increase in bedrock chemical weathering upsection due to leaching of calcium-bearing mafic minerals[18]. **b**, Bedrock CaO content with bulk (crosses) or sporadic (dots) enrichments. Grey crosses represent bulk-enriched targets but where distinction of fracture-fill veins remains ambiguous from available images. Vertical grey lines highlight average bedrock composition (1.6 wt% CaO), with 30 and 50% calcium sulfate (bassanite) enrichments. **c**, Occurrence of fracture-fill veins for vertical and horizontal orientations as percentage of the number of workspace images with bedrock (Supplementary Fig. 12). Light grey indicates that at least one vein is visible, and dark grey corresponds to a higher density of veins; horizontal bars represent the uncertainty of the average. **d**, Bedrock MgO/SiO$_2$ content ratio (same data as in Fig. 2b,c). Error bars represent root mean square error (RMSE) for the MgO/SiO$_2$ content ratio. The purple horizontal bar represents the elevation range where image data show the magnesium sulfate-enriched lithology (Supplementary Fig. 7). Location of Old Soaker[34] and other candidate desiccation cracks (Supplementary Fig. 13). **e**, Average normalized chlorine peak area associated with halite detections (Supplementary Fig. 10)[31]; error bar represents the uncertainty of the average.

with an average CaO content ~1.6 wt%) with 30–50 wt% of a calcium sulfate end-member (Fig. 2a; see also Supplementary Fig. 1 and Supplementary Table 1). For such concentrations, the signal is clearly expressed in emission spectra by three peaks at 543, 545 and 564 nm, leading to a ~0.2-nm shift in the location of peak centroids at 543 and 545 nm, combined with an increase in the magnitude of the 564-nm peak emission (Supplementary Fig. 2), as observed in laboratory experiments[19]. Independent measurement by the Alpha Particle X-ray Spectrometer (APXS) at the centimetre scale also recorded bulk CaO enrichments of the Murray bedrock that are correlated with SO$_3$ content, toward the CaSO$_4$ end-member (Supplementary Fig. 3).

Calcium sulfate corresponding to bedrock enrichment excludes contribution from mineralized veins identified from images taken at <0.5 mm per pixel using the ChemCam Remote Micro Imager (RMI). In the absence of vein contribution, the repeated enrichment in the majority of observation points within both sandstone and mudstone targets indicates that the enrichment is disseminated within the bulk rock (Supplementary Table 1 and Fig. 3). In general, the mudstone is laminated[20]; however, intervals with calcium sulfate enrichment are commonly more resistant to erosion and display nodular or massive textures (Fig. 3 and Supplementary Figs. 4 and 5). Where close-up images (<100 μm per pixel) are available these intervals do not show veins (Fig. 3e), although in some cases

submillimetre white grains (Fig. 3f) or elongate euhedral crystals associated with crystal moulds (Fig. 3g) were observed. Bulk enrichment occurs at several discrete elevations between −4,370 and −4,200 m in the stratigraphy of the upper Murray formation, contrasting with only sporadic enrichment detected elsewhere in the formation (Fig. 1b).

The association of calcium with carbonate, which neither ChemCam nor APXS can directly detect, cannot be entirely ruled out (Fig. 2a shows that bedrock CaO content increases by up to ~8 wt% while sulfur remains below detection limits, which could allow for up to ~12 wt% calcite). Nevertheless, X-ray diffraction analyses on Murray bedrock drill samples confirmed the absence of carbonates (<1 wt%) and the presence of clay and calcium sulfate[12]. An association between CaO and sulfate is also clearly observed (Supplementary Fig. 3), suggesting that no substantial calcite is present in the Murray formation.

An interval with magnesium sulfates

In addition to calcium sulfate, magnesium sulfate bedrock enrichments occur in a relatively thin (<10 m) stratigraphic interval within the heterolithic Sutton Island member (Fig. 1d, purple bar). On sol 1690 (elevation −4,287 m), ChemCam analysis of unusual, brown-coloured bedrock fragments within the Murray mudstone showed a distinct enhancement of magnesium, sulfur and hydrogen.
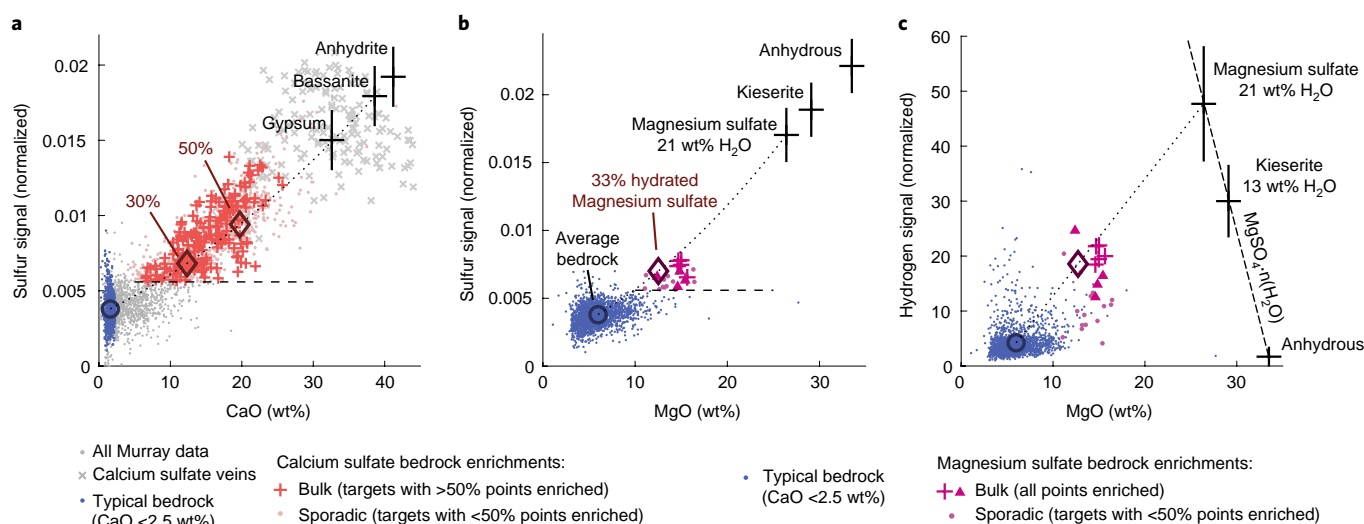
Fig. 2 | ChemCam oxide and elemental data of calcium and magnesium sulfate enrichments. a–c, Sulfur signal as a function of CaO (**a**) and MgO (**b**) content, and hydrogen signal as a function of MgO content (**c**), for typical Murray bedrock with CaO <2.5 wt% (blue) and for sulfate enrichments. **a**, For calcium sulfates (red), sulfur signal above the limit of detection (dashed line, SO_3 >10.6 wt%) and CaO > 5 wt%. Mixtures at 30 and 50% (diamonds) of calcium sulfate with average typical bedrock (circle) are shown with the binary mixing trend (dotted line) and end-members (black crosses). **b,c**, Magnesium sulfate enrichments (purple), defined by sulfur signal above the limit of detection, and MgO >10 wt%, found disseminated in the Norwood Cove (crosses) and Beach Cliff (triangle) bedrock fragments (Supplementary Fig. 6), and compared to 33% hydrated magnesium sulfate mixture (diamond) with average bedrock (Supplementary Table 2). Dashed line in **c** represents magnesium sulfate with varying water content. Vertical error bars on end-members represent sulfate (**a,b**) and water content (**c**) calibration uncertainties.

The estimated composition is interpreted as a binary mixture between a hydrated magnesium sulfate end-member and typical bedrock of the Murray formation (Fig. 2b,c and Supplementary Fig. 1). The analysed fragments have a bulk water content of 8.6 ± 1.9 wt%, estimated from the hydrogen signal[21], which is significantly higher than typical Murray bedrock (1.6 wt%). The lack of calcium sulfate enrichment in these rocks is reflected in a very low CaO content (Supplementary Fig. 1). The magnitude of the sulfur signal is consistent with $18.4^{+4.0}_{-4.8}$ wt% average sulfate content based on measurements of the Norwood Cove fragment (Supplementary Fig. 6) with 1-sigma uncertainty, corresponding to a bulk content of 33 wt% hydrated magnesium sulfate (1-sigma lower bound is 26 wt%; Supplementary Table 2).

Magnesium sulfate-enriched lithologies occur in planar exposures of relatively erosion-resistant rocks. The outcrop is poorly preserved and consists of broken, metre-scale blocks separated by unconsolidated fines. Relative to surrounding lithologies, strata with magnesium sulfate enrichment have a reddish-brown colour, are variably fractured, show a typical nodular to massive texture (Supplementary Fig. 7) and weather into centimetre-sized angular fragments (such as the Norwood Cove and Beach Cliff targets; see Supplementary Fig. 6). The grain size of these magnesium sulfate-enriched rocks is silt-sized or smaller, on the basis of compositional homogeneity of the ChemCam data (Supplementary Fig. 8), and is similar to grain sizes estimated for surrounding Murray bedrock[22]. At several locations, this lithology is exposed in large contiguous blocks and confined to centimetre-thick planar exposures that are evenly interbedded with finely laminated Murray mudstone (Fig. 3a). The lateral extent of magnesium sulfate-enriched exposures is uncertain, because of the lack of high-resolution image coverage and the scattered nature of bedrock exposures (Supplementary Fig. 7). The maximum lateral distance observed in images is 4 m. Sporadic magnesium sulfate detections were also observed over 30 of thickness of heterolithic facies above (Fig. 1d).

The magnesium sulfate-enriched rocks were not examined by the APXS, but high thermal neutron count rates, recorded by the dynamic albedo of neutrons (DAN) instrument in the same area (Supplementary Fig. 9), support the presence of elevated bedrock hydration within this stratigraphic interval. A signature consistent with a hydrated sulfate phase is also recorded on the site from orbit: hydration and hydrated sulfate spectral indices are enhanced in the portion of the Murray formation where magnesium sulfate-enriched lithologies were observed in situ, and the signature was less clear or absent in bedrock exposures below that interval (Supplementary Fig. 11). The hydrated sulfate signature also extends laterally at similar elevation to either side of the rover traverse.

Timing of enrichment and formation scenario

Understanding the timing of bedrock sulfate enrichment is crucial to deciphering its environmental implication. Enrichments have not been observed in the form of large, continuous beds of nearly pure salt, as could be expected for evaporite minerals formed as cumulates or as lake bottom-growth deposits. In available images of bedrock, no features were observed that clearly indicate primary salts, their dissolution or the presence of disruptive fabrics common to terrestrial evaporitic settings[23].

Although a late-diagenetic origin for calcium and magnesium sulfate enrichments cannot be uniquely discounted, we believe that such an origin is unlikely. Local bedrock does not appear to show a greater abundance of mineralized fractures (Fig. 3 and Supplementary Figs. 4 and 5), and sulfate enrichments are disseminated in the host rock and do not correlate with the late-diagenetic fractures mineralized by calcium sulfate[13] (Supplementary Fig. 5). Additionally, the presence of mineralized veins within typically sulfate-poor Murray bedrock suggests that bedrock porosity was sufficiently reduced and that later diagenetic fluids were confined to fracture systems.

Early diagenetic precipitation from saline brines, followed by recrystallization during burial and exhumation, is in line with the observed geochemistry and textures. In particular, the disseminated sulfate enrichments are restricted to a specific stratigraphic interval, where they occur as repetitive discrete horizons (Fig. 3). In this
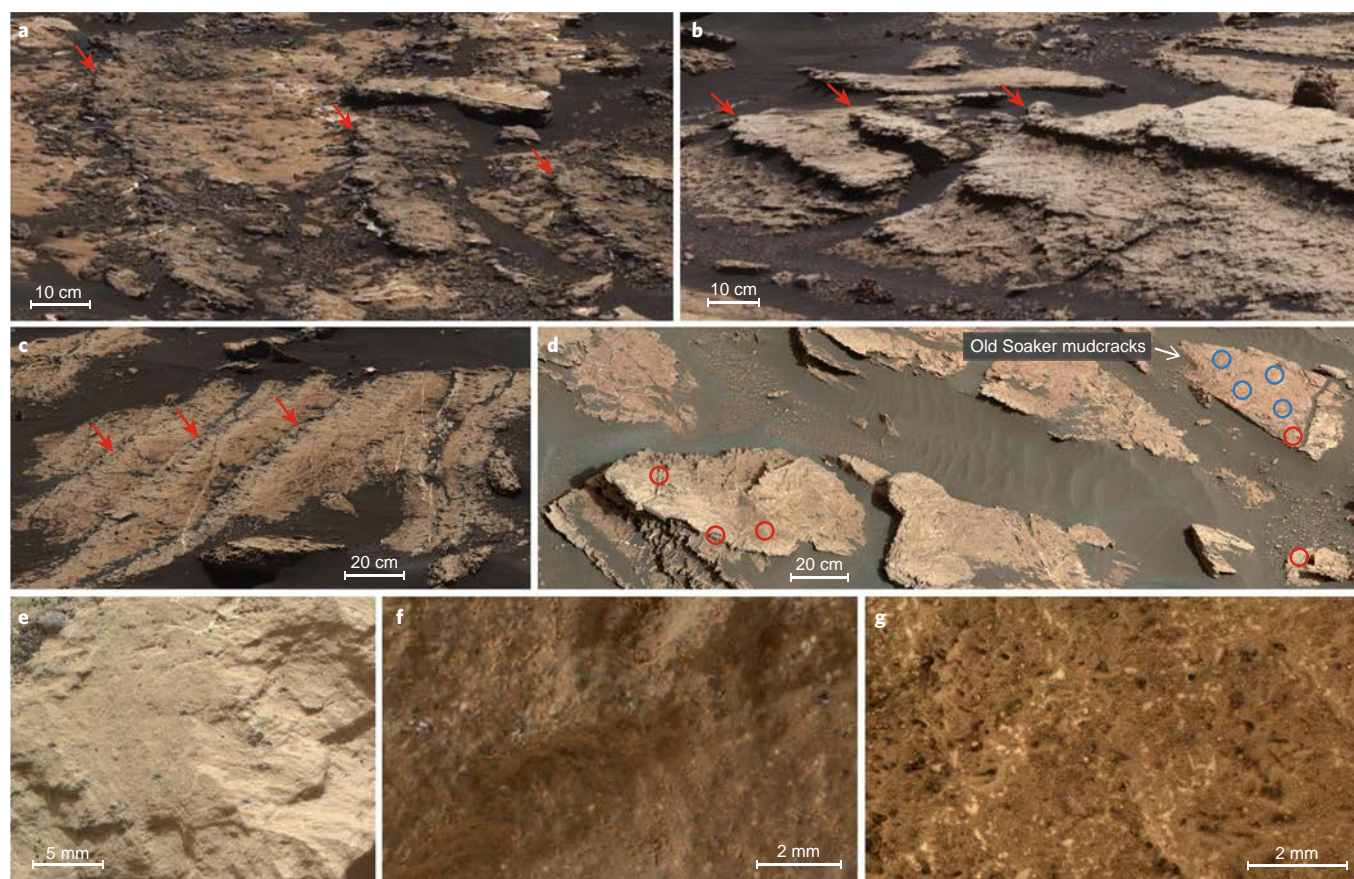
Fig. 3 | Lithology of sulfate enrichments. a, Magnesium sulfate-enriched lithology within multiple parallel horizons (red arrows) on a large block of bedrock (mcam08715). **b**, Calcium sulfate enrichments as erosion-resistant horizons (red arrows) in mudstone (mcam08669; Supplementary Fig. 4a). **c**, Multiple horizons (red arrows) where euhedral white crystals (Supplementary Fig. 4g) and heterogeneous calcium sulfate and magnesium sulfate enrichments were observed (mcam08733). **d**, Exposed blocks at Old Soaker with desiccation cracks[34] (Supplementary Fig. 13a) (mcam07752); circles represent the locations of ChemCam targets with calcium sulfate enrichments (red) and without (blue). **e,f**, Close-up MAHLI images of a mudstone (**e**, Lookout Point, Supplementary Fig. 5a) and a sandstone enriched in calcium sulfate (**f**, 1710MH0001220010604335C00; White Ledge, Supplementary Fig. 5c). **g**, Close-up MAHLI image of bedrock with white euhedral crystals along with empty casts/moulds (1679MH0001930000603555R00; Supplementary Fig. 4d).

scenario, episodic saturation of sulfate-rich brines resulted in the early diagenetic precipitation of sulfate salts within shallow sediments (Fig. 4). Such subsurface crystallization can occur either during subaerial exposure resulting in evaporative enrichment in the capillary fringe, or subaqueously as dense, super-saturated brines diffuse downward into the sediment pore space[24]. The estimated 30–50 wt% of calcium sulfate enrichment is consistent with intra-sediment crystallization in poorly compacted sediment[25]. Similar deposition could have occurred with magnesium sulfates where brines became much more concentrated by evaporation (Fig. 4). The estimated proportion of 26–36 wt% magnesium sulfate initially represents 38–50% by volume, assuming precipitation of epsomite $(MgSO_4 \cdot 7H_2O)$ in pores of siliciclastic sediment with grains of approximately basalt density (~3.0 g cm^{-3}), again implying growth in poorly compacted sediments.

Sulfate enrichment within discrete beds of limited lateral extent in the heterolithic mudstone–sandstone facies indicates that salts were probably deposited along shallow lake margins, possibly within multiple ponds fed by distributive channel systems and groundwaters (Fig. 4). Magnesium sulfate enrichment, which is confined to relatively small stratigraphic intervals, occurs in horizons discretely separate from calcium sulfate, suggesting that magnesium sulfate-rich brines were physically fractionated from the fluid that formed calcium sulfates as the brine concentrated downstream. Changes

in seasonal temperature and humidity cycling during post-depositional exposure of such hydrated sulfate salts would have exposed these materials to repeated changes in hydration state and dissolution. In the absence of complete dissolution, volumetric changes associated with changes in hydration state are expected to disrupt initial depositional textures[26,27].

After deposition, the Murray formation was probably buried to ~1 km[9], which itself may have triggered a change in calcium sulfate hydration state[28,29]. Following compaction and lithification, late-stage fluids deposited calcium sulfate within fractures. Horizontal and subhorizontal veins occur specifically in the stratigraphic interval with the enrichments (Fig. 1c), a setting similar to terrestrial satin spar veins associated with primary calcium sulfate deposits[30]. These late calcium sulfate fluids were likely to have partially mobilized highly soluble salts within the bedrock, such as halite. Indeed, enhanced sodium chloride detections occur at specific stratigraphic intervals (Fig. 1e and Supplementary Fig. 10), and their sporadic distribution in bedrock and occasionally in association with fracture-filling calcium sulfates indicates remobilization[31]. Locally, lateral variation and possible cross-cutting of magnesium sulfate enrichment occurs at the centimetre/decimetre scale (Supplementary Fig. 7), as well as sporadic detections of magnesium sulfate near the stratigraphic succession (Fig. 1d), which may also reflect localized dissolution and re-precipitation of initial deposits (Fig. 1d).
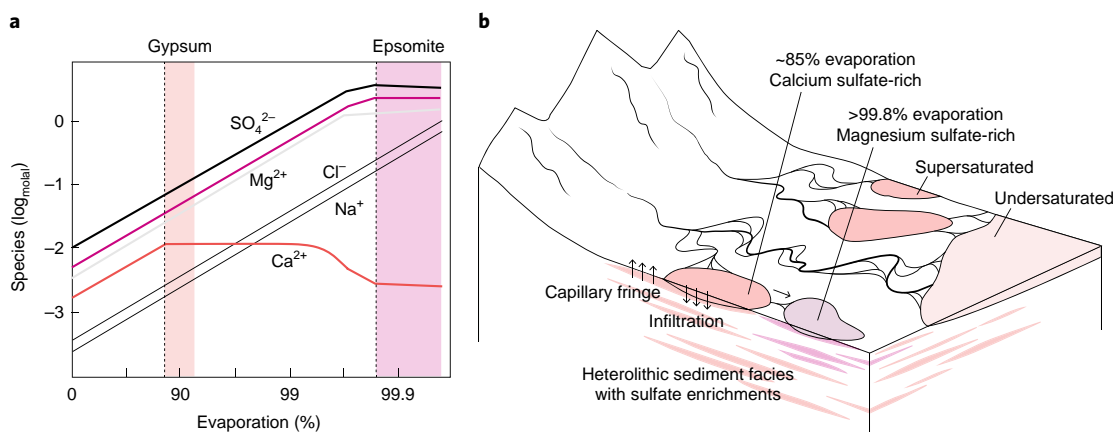
Fig. 4 | Evaporation of surface brines and early diagenetic deposition. a, Evaporation of basaltic weathering-derived fluids leads to major precipitation of calcium sulfates, first such as gypsum (red), and then magnesium sulfates such as epsomite (purple) within the shaded ranges of evaporation[3]. The evolution of iron species, which are dependent on pH, does not significantly change calcium and magnesium sulfate precipitation[3] and is not shown here because iron is relatively immobile (found in iron oxides, clays and amorphous phases). **b**, Schematic of a deposition scenario in the margin of the Gale lake basin, possibly forming several over-filled or evaporative ponds fed by distributive fluvial systems and consistent with the heterolithic mudstone–sandstone facies observed in the upper Murray formation[41]. Brine crystallizes in the shallow sediment pore space, either by subaqueous infiltration or within capillary fringes where occasional subaerial exposure occurs.

Nevertheless, while calcium sulfate-enriched fluids would readily mobilize halite, magnesium sulfate-enriched bedrock could persist even though magnesium sulfate is soluble, because SO_4^{2-} ions released during dissolution would immediately trigger the formation of less soluble calcium sulfate, which could shield magnesium sulfates from further dissolution.

Following exhumation and exposure of the Murray formation to the temperatures and relative humidity of modern Mars, hydrated magnesium sulfate minerals turn to amorphous phases of various hydration states. The calculated 21 wt% water associated with the magnesium sulfate phase (Fig. 2c and Supplementary Table 2) corresponds to a hydration state of 1.8 H_2O per $MgSO_4$, and is consistent with the predicted amorphous desiccation products of epsomite or hexahydrite[26,32]. The intensely fractured and broken nature of magnesium sulfate-enriched rocks may reflect diurnal and seasonal cycles of dehydration–rehydration[33].

Overall, geochemical and textural data are consistent with sulfate enrichment in this interval by early diagenetic precipitation from saline waters, although unambiguous sedimentary structures (for example, nodular displacive fabrics) are not observed. This may have resulted from either the scarcity of high-resolution images acquired in this interval or the post-depositional alteration of primary depositional textures. Importantly, however, features other than sulfate enrichments indicate lowering of lake levels and intermittent evaporative conditions in this part of the Murray formation. First, desiccation cracks are identified in the stratigraphy at Old Soaker[34] and possibly at several other locations (Supplementary Fig. 11) in close proximity to the strata containing sulfate enrichment (Fig. 1d). At Old Soaker, calcium sulfate enrichment occurs in sandstone adjacent to the mudcracks (Fig. 3d). Second, elevated concentration of sodium chloride in the bedrock is also observed, relative to stratigraphically lower strata[31]. Sodium chloride occurrences in specific intervals, close to sulfate enrichments, suggests remobilization from layers potentially enriched in halite (Fig. 1e). Third, the first occurrence of calcium sulfate enrichment coincides with a previously reported change in clay mineralogy, consistent with episodic wetting and drying of lake environments[12] and increased chemical weathering of the bedrock detrital component[18] (Fig. 1). In Gale's closed-basin hydrology,

leached ions would accumulate in waters and, following evaporation, create brines that precipitate salts such as calcium and magnesium sulfates.

Hydrological and climatic variability

The observed calcium/magnesium sulfate and chloride assemblages are predicted to have resulted from alteration of Martian basalts to produce sulfate- and chloride-rich, but iron-poor, brines[1]. The relatively low solubility of calcium sulfate minerals results in their widespread production during evaporation, while less common magnesium sulfate and chloride minerals represent terminal evaporation. Iron oxides are observed in visible/near-infrared spectral data and X-ray diffraction of Murray bedrock samples[28,35], yet there is no evidence for iron sulfate enrichments in this interval, probably because iron is not mobile in solution, indicating that saline waters were either oxidizing or not acidic. While calcium sulfate enrichment is observed, calcite is absent from the stratigraphy—that is, not detected by CheMin at its threshold of 1 wt%. This could have resulted from either low alkalinity or low atmospheric CO_2, or an environment where precipitation of calcite was otherwise inhibited[36]. Besides, the presence of calcium sulfate means that previous $CaCO_3$ formation (if any) was insufficient to deplete calcium from solution. Our findings do not compromise the search for life in Gale crater; terrestrial magnesium sulfate-rich hypersaline lakes are known to accommodate halotolerant biota[37–39], and crystallization of sulfate salts may also aid preservation of biosignatures[40].

Previous observations suggest that different lake depths were recorded in the lower Murray formation[10]. In the upper part of the formation, where clear rock exposures are more scarce, sedimentary structures suggest deposition in lake-margin environment with potential episodes of desiccation[34,41,42]. Our discovery of sulfate deposits is consistent with episodic desiccation. The limited lateral extent of sulfate-enriched beds also suggests the potential for segmentation of the Gale lake into discrete ponds, including those where extremely evapo-concentrated brines might form (Fig. 4). Changes in lake level are an anticipated response within closed-basin lakes to variation in the regional hydrological budget. In addition, over time, intervals for lacustrine deposition of ~1 million years ago or less, based on plausible sedimentary deposition

rates[9], Mars experiences significant changes in obliquity and orbital eccentricity driving cyclical climate fluctuations[43]. Alternatively, a drier Gale lake might be a sign of long-term, secular global drying of Mars, posited based on orbital observations[5].

The interval discussed here preserves the first occurrence of significant sulfate-enriched bedrock (>30 wt% sulfate with siliciclastics) in Gale crater's sedimentary record. As the rover continues to traverse upsection toward successively younger rocks, key questions include the prevalence of similar bedrock sulfate enrichments. If thin stratigraphic intervals with salt enrichments or sedimentological evidence for aridity continue to occur, cyclical or episodic processes are a plausible underlying cause. If, on the other hand, sulfate-enriched intervals increase in frequency and thickness, perhaps incorporating observable displacive fabrics and pure sulfate beds, the enrichments investigated here may be a harbinger of the long-term, secular drying of Mars. This has been hypothesized for the Mount Sharp sulfate unit observed from orbit further upsection[8] and deposits elsewhere on Mars[5]. As the rover continues its traverse towards this sulfate unit, it will therefore be crucial to recognize sulfate-enriched bedrock in reconnaissance observations, to obtain accompanying high-resolution stereo images of textures and drill samples for X-ray diffraction, evolved gas and isotopic analyses.

Online content

References

1. Tosca, N. J. & McLennan, S. M. Chemical divides and evaporite assemblages on Mars. *Earth Planet. Sci. Lett.* **241**, 21–31 (2006).
2. Clark, B. C. et al. Chemistry and mineralogy of outcrops at Meridiani Planum. *Earth Planet. Sci. Lett.* **240**, 73–94 (2005).
3. Tosca, N. J. et al. Geochemical modeling of evaporation processes on Mars: insight from the sedimentary record at Meridiani Planum. *Earth Planet. Sci. Lett.* **240**, 122–148 (2005).
4. Ehlmann, B. L. & Edwards, C. S. Mineralogy of the Martian surface. *Annu. Rev. Earth Planet. Sci.* **42**, 291–315 (2014).
5. Bibring, J.-P. et al. Global mineralogical and aqueous Mars history derived from OMEGA/Mars express data. *Science* **312**, 400–404 (2006).
6. Le Deit, L. et al. Sequence of infilling events in Gale Crater, Mars: results from morphology, stratigraphy, and mineralogy. *J. Geophys. Res. Planets* **118**, 2439–2473 (2013).
7. Fraeman, A. A. et al. The stratigraphy and evolution of lower Mount Sharp from spectral, morphological, and thermophysical orbital data sets. *J. Geophys. Res. Planets* **121**, 1713–1736 (2016).
8. Milliken, R. E., Grotzinger, J. P. & Thomson, B. J. Paleoclimate of Mars as captured by the stratigraphic record in Gale Crater. *Geophys. Res. Lett.* **37**, (2010).
9. Grotzinger, J. P. et al. Deposition, exhumation, and paleoclimate of an ancient lake deposit, Gale crater, Mars. *Science* **350**, aac7575 (2015).
10. Hurowitz, J. A. et al. Redox stratification of an ancient lake in Gale crater, Mars. *Science* **356**, eaah6849 (2017).
11. McLennan, S. M. et al. Elemental geochemistry of sedimentary rocks at Yellowknife Bay, Gale Crater, Mars. *Science* **343**, 1244734 (2014).
12. Bristow, T. F. et al. Clay mineral diversity and abundance in sedimentary rocks of Gale crater, Mars. *Sci. Adv.* **4**, eaar3330 (2018).
13. Nachon, M. et al. Calcium sulfate veins characterized by ChemCam/Curiosity at Gale crater, Mars. *J. Geophys. Res. Planets* **119**, 2013JE004588 (2014).
14. Rapin, W. et al. Hydration state of calcium sulfates in Gale crater, Mars: identification of bassanite veins. *Earth Planet. Sci. Lett.* **452**, 197–205 (2016).
15. Kah, L. C., Stack, K. M., Eigenbrode, J. L., Yingst, R. A. & Edgett, K. S. Syndepositional precipitation of calcium sulfate in Gale Crater, Mars. *Terra Nova* **30**, 431–439 (2018).
16. Nachon, M. et al. Chemistry of diagenetic features analyzed by ChemCam at Pahrump Hills, Gale crater, Mars. *Icarus* **281**, 121–136 (2017).
17. VanBommel, S. J. et al. Deconvolution of distinct lithology chemistry through oversampling with the Mars Science Laboratory Alpha Particle X-Ray Spectrometer. *Xray Spectrom.* **45**, 155–161 (2016).
18. Mangold, N. et al. Chemical alteration of fine-grained sedimentary rocks at Gale crater. *Icarus* **321**, 619–631 (2019).
19. Anderson, D. E. et al. Characterization of LIBS emission lines for the identification of chlorides, carbonates, and sulfates in salt/basalt mixtures for the application to MSL ChemCam data. *J. Geophys. Res. Planets* **122**, 744–770 (2017).
20. Stack, K. M. et al. Evidence for plunging river plume deposits in the Pahrump Hills member of the Murray formation, Gale crater, Mars. *Sedimentology* **0**, (2018).
21. Rapin, W. et al. Quantification of water content by laser induced breakdown spectroscopy on Mars. *Spectrochim. Acta Part B At. Spectrosc.* **130**, 82–100 (2017).
22. Rivera-Hernández, F. et al. Using ChemCam LIBS data to constrain grain size in rocks on Mars: proof of concept and application to rocks at Yellowknife Bay and Pahrump Hills, Gale crater. *Icarus* **321**, 82–98 (2019).
23. Warren, J. K. *Evaporites: Sediments, Resources and Hydrocarbons* (Springer Science & Business Media, 2006).
24. Handford, C. R. in *Developments in Sedimentology*, Vol. 50 (ed. Melvin, J. L.) 1–66 (Elsevier, 1991).
25. Giles, M. R. *Diagenesis: A Quantitative Perspective: Implications for Basin Modelling and Rock Property Prediction* (Kluwer Academic, 1997).
26. Chipera, S. J. & Vaniman, D. T. Experimental stability of magnesium sulfate hydrates that may be present on Mars. *Geochim. Cosmochim. Acta* **71**, 241–250 (2007).
27. Holliday, D. W. The petrology of secondary gypsum rocks: a review. *J. Sediment. Res.* **40**, 734–744 (1970).
28. Vaniman, D. T. et al. Gypsum, bassanite, and anhydrite at Gale crater, Mars. *Am. Mineral.* **103**, 1011–1020 (2018).
29. Schieber, J. et al. Encounters with an unearthly mudstone: understanding the first mudstone found on Mars. *Sedimentology* **64**, 311–358 (2017).
30. Gustavson, T. C., Hovorka, S. D. & Dutton, A. R. Origin of satin spar veins in evaporite basins. *J. Sediment. Res.* **64**, 88–94 (1994).
31. Thomas, N. H. et al. Mars Science Laboratory Observations of Chloride Salts in Gale Crater, Mars. *Geographic. Res. Lett.* https://doi.org/10.1029/2019GL082764 (2019).
32. Wang, A., Freeman, J. J. & Jolliff, B. L. Phase transition pathways of the hydrates of magnesium sulfate in the temperature range 50°C to 5°C: implication for sulfates on Mars. *J. Geophys. Res. Planets* **114**, E04010 (2009).
33. Vaniman, D. T. & Chipera, S. J. Transformations of Mg- and Ca-sulfate hydrates in Mars regolith. *Am. Mineral.* **91**, 1628–1642 (2006).
34. Stein, N. et al. Desiccation cracks provide evidence of lake drying on Mars, Sutton Island member, Murray formation, Gale Crater. *Geology* **46**, 515–518 (2018).
35. Chemcam passive reflectance spectroscopy of recent drill tailings, hematite-bearing rocks, and dune sands. *in* **47**, 1155 (2016).
36. Tosca, N. J., Ahmed, I. A. M., Tutolo, B. M., Ashpitel, A. & Hurowitz, J. A. Magnetite authigenesis and the warming of early Mars. *Nat. Geosci.* **11**, 635 (2018).
37. Cabestrero, Ó., del Buey, P. & Sanz-Montero, M. E. Biosedimentary and geochemical constraints on the precipitation of mineral crusts in shallow sulphate lakes. *Sediment. Geol.* **366**, 32–46 (2018).
38. Kilmer, B. R. et al. Molecular and phenetic characterization of the bacterial assemblage of Hot Lake, WA, an environment with high concentrations of magnesium sulfate, and its relevance to Mars. *Int. J. Astrobiol.* **13**, 69–80 (2014).
39. Pontefract, A. et al. Microbial diversity in a hypersaline sulfate lake: a terrestrial analog of ancient Mars. *Front. Microbiol.* **8**, 1819 (2017).
40. Aubrey, A. et al. Sulfate minerals and organic compounds on Mars. *Geology* **34**, 357–360 (2006).
41. Fedo, C. et al. Sedimentology and stratigraphy of the Murray formation, Gale crater, Mars. In *49th Lunar and Planetary Science Conference 2018*, 2078 (Lunar Planetary Institute, 2018).
42. Schieber, J. et al. A sand-lens in the upper Murray formation at Gale crater, Mars: a likely lowstand deposit of a dynamic ancient lake. *in* **48**, 2311 (2017).
43. Laskar, J. et al. Long term evolution and chaotic diffusion of the insolation quantities of Mars. *Icarus* **170**, 343–364 (2004).

Acknowledgements

Author contributions

W.R. analysed the LIBS and image data and conceived and wrote the manuscript. W.R., B.L.E. and G.D. conceived and revised the manuscript. J.S., W.W.F., B.C.C., L.C.K., N.M., R.C.W. and A.R.V., contributed to the interpretation of the data and revisions of the manuscript. N.H.T. provided LIBS chloride peak analyses. V.K.F. analysed CRISM signatures of hydrated sulfates. N.T.S. and F.R.H. provided grain size estimates from Mars Hand Lens Imager (MAHLI) images of Murray bedrock. M.N. and H.A.M. identified and mapped sulfate vein occurrences. L.T. analysed APXS data of Murray bedrock. T.S.J.G. and C.H. provided DAN data analysis.

Competing interests

The authors declare no competing interests.

Additional information

Supplementary information is available for this paper at https://doi.org/10.1038/s41561-019-0458-8.

Correspondence and requests for materials should be addressed to W.R.

Peer review information Primary handling editor(s): Stefan Lachowycz.

Reprints and permissions information is available at www.nature.com/reprints.

Publisher's note Springer Nature remains neutral with regard to jurisdictional claims in published maps and institutional affiliations.

Methods

Rover-based geochemical datasets and data processing. The MSL has five instruments that can measure geochemistry and mineralogy[44]. Because of the rover traverse path and rate at the time, APXS, CheMin and SAM data were not acquired of the magnesium/sulfur/hydrogen-enriched strata, so ChemCam is the primary source of chemical data used along with hydration of the upper ~0.5 m of the surface probed by the DAN instrument. The latter is a neutron spectrometer, sensitive to thermal and epithermal neutrons, and is regularly operated in active and passive modes throughout the traverse. The count rate of thermal neutrons in passive mode (data shown in Supplementary Fig. 9) can be elevated due to either the presence of neutron scatterers (predominantly hydrogen) or the paucity of neutron absorbers (predominantly chloride and iron)[45]. On the other hand, ChemCam is a laser-induced breakdown spectrometer (LIBS) that provides chemical analyses at a submillimetre scale and detailed images with the RMI[46,47]. Major-element contents were obtained using the current calibration model[48]. Water and sulfate content was estimated using dedicated calibration models[21] for water content quantification based on the hydrogen signal; see below for a description of the sulfur signal calibration used in this study.

The ChemCam dataset used here includes bedrock targets of the Murray formation. A subset of bedrock observations was selected from all ChemCam observations based on: (1) image classification to select only bedrock analyses and remove potential contribution from soils or diagenetic features such as light-toned fracture-fill veins; and (2) signal strength to keep points above a minimum total spectral intensity ($>1.6 \times 10^{14}$ photons) for which noise level is acceptable for sulfur peak analyses. An additional selection is made based on major-element oxide contents to separate points that indicate contributions from calcium sulfate-, silica- or iron-rich features to represent typical bedrock composition (Fig. 2 and Supplementary Fig. 1). The threshold for rejection due to calcium sulfate enrichment was defined at 2.5 wt% CaO from the distribution of bedrock observations, which shows that measurements group tightly around 1.6 wt% CaO, with sporadic enrichments above 2.5 wt% (Supplementary Fig. 3) related to increased signal (Supplementary Fig. 2). The APXS instrument independently measures centimetre-scale bulk compositions and demonstrates the association of calcium and sulfur in Murray bedrock observations. The CaO content measured by APXS ranges from 2 to 25 wt%, and is correlated with SO_3 content along the 1/1 stoichiometric ratio of calcium sulfate (Supplementary Fig. 3). Given the correlation observed on APXS data down to 2 wt% CaO, the slightly lower CaO abundance of the cluster defined by ChemCam data is most probably related to its ability to examine bedrock free of dust and without calcium sulfate enrichments with its 0.3–0.5-mm analytical footprint compared to the 17-mm footprint of APXS.

Estimation of sulfate content from ChemCam data. The SO_3 content is estimated from the sulfur signal observed in ChemCam spectra. The challenge with the measurement of the signal is that the sulfur emission peaks present in ChemCam spectra are relatively weak in comparison to nearby interfering iron emission peaks[13], necessitating a distinct method for their quantification compared to the major oxides. While others have investigated the calibration of with LIBS[49–51], here we used a distinct approach dedicated to data collected in situ on sulfates within the Murray bedrock. This approach shows, based on laboratory data, that spectral parameters can be defined to identify and differentiate the sulfur signal from other interfering spectral features, including identification of the threshold of wt% at which it becomes apparent. Second, the sulfur signal identified on Mars is calibrated in situ using a large set of Murray bedrock measurements containing calcium sulfate enrichments.

Collection of laboratory reference spectra. The ChemCam testbed at Los Alamos National Laboratory was used to collect data from pelletized mixtures of calcium and magnesium sulfates with basalt[19]. Additional magnesium sulfate pressed pellets were also prepared to resolve sulfur signal variation closer to the limit of detection and compositional range observed in the enrichments at Gale crater. The same basalt as that in ref. [19] was used (K1919 basalt sieved powder, <45 μm), but it was doped with 7 wt% sieved haematite powder (<45 μm) so that the mixture had a total iron content of 19 wt%, closer to the bedrock composition of the Murray formation at Gale crater. The magnesium sulfate powder was a synthetic reagent, the same as used in ref. [19], obtained from Macron Chemicals (CAS 7487-88-9), and was mixed in various proportions with the basalt-haematite powder (Supplementary Table 3). The powder mixture pellets were each analysed with eight observation points of 30 laser shots each.

Processing and measurement of emission peaks. Iron peaks interfere significantly with sulfur emission peaks at ~543 nm (S II at 543.02 nm and S II at 543.43 nm forming a single peak in ChemCam spectra) and 545.53 nm, but the sulfur still produces specific spectral peak features when present. The sulfur signal can be distinguished using the position of the spectral peak centroid computed from, respectively, ten and eleven spectral bins on the two specific locations after baseline correction (Supplementary Fig. 14). The sulfur emission peak area at ~564 nm (multiple S II peaks forming a single peak in ChemCam spectra), with minor silicone and iron emission peak interferences, is then used to evaluate sulfur signal

intensity. This is then normalized to the oxygen emission peak area at ~778 nm (O I at 777.41, 777.63 and 777.75 nm forming a single peak). Sulfur and oxygen peak areas are obtained by integrating the spectral bins after baseline correction. As shown on Fig. 2, the increase in sulfate abundance and associated decrease in emission of other peaks from breakdown of the basalt matrix produces a specific shift to longer wavelengths for the spectral centroids at ~543 and ~545 nm, with a simultaneous increase in the normalized peak area at ~564 nm. Using this approach, laboratory data suggest a threshold of sulfate detectability around 10 wt% sulfate, with the possibility of obtaining a still lower threshold by more refined fitting and/or multivariate spectral fitting procedures.

Calibration of the signal. abundance estimates based on the 564-nm peak area are calibrated with in situ sulfate data collected on Mars. Indeed, bedrock of the upper Murray formation has a rather low bulk CaO content, but a large number of CaO enrichments were observed at the LIBS scale, related to calcium sulfates. The association of sulfur with calcium is observed because the data from Murray bedrock, after removal of other iron- and magnesium-rich diagenetic features, follow the same trend of peak area increase at ~564 nm and centroid shifts observed in the laboratory. Additionally, measurements from the APXS instrument independently confirm the correlation of CaO with SO_3 content in the upper Murray formation (Supplementary Fig. 3). The SO_3 content calibration curve for the normalized peak area at ~564 nm (Fig. 2f) is obtained by attributing CaO enrichments from average bedrock >2.5 wt% CaO to calcium sulfate.

This in situ calibration curve obtained using calcium sulfate data can then be used to predict sulfate content related to magnesium sulfates, because tests in the laboratory have shown that for both magnesium and calcium sulfates the normalized peak area increases along the same calibration curve and up to the same normalized peak area value for the pure sulfate pellets (Fig. 2c). The limit of detection on sulfate content using this approach is calculated from the 95% confidence bound of the calibration curve. Its intercept has a normalized peak area that corresponds to a predicted 10.6 wt% SO_3 content. Data from the upper Murray show that MgO enrichments are correlated with the normalized peak area at ~564 nm, as well as centroid shifts (Fig. 2), which confirms the presence of sulfate from the signal. The current calibration model used to estimate major oxide content[48] is not yet optimized to include magnesium sulfate-bearing basaltic mixtures and, consequently, the total amount of oxides predicted exceeds 100% after water and sulfate content are included. This was also found to be the case when laboratory magnesium sulfate-bearing basaltic mixture major elements were calculated using the current calibration model. Consequently, assuming that the proportions predicted for the major oxides are correct, the oxide amounts are then re-normalized to account for water and sulfate content, so that the total is 100%.

Identification of magnesium sulfate-enriched lithology. A correlation was identified between the occurrence of magnesium sulfates in LIBS data on sol 1680 (Supplementary Fig. 5) and the specific lithology observed on Murray bedrock in colour image data (Supplementary Fig. 7). MastCam images of bedrock or blocks of bedrock were analysed to identify the magnesium sulfate-enriched lithology with characteristics defined by (1) its texture: nodular or massive, erosion resistant, forming centimetre-thick layers in some cases; (2) its weathering style: cracking in poorly rounded, centimetre-sized chunks that remain more resistant to erosion than typical Murray bedrock; and (3) its colour: brown relative to typical Murray bedrock. The specific colour was identified and mapped on MastCam images to verify that the same colour was observed for the lithology at the various sites visited.

Colour identification. Red–green–blue pixel values of radiometrically corrected MastCam images were converted into CIE $L^*a^*b^*$ colour space, with L^* lightness, and a^* and b^* colour parameters (Supplementary Fig. 15). This determined the colour and lightness parameters interval for the fragments of bedrock where magnesium sulfate enrichments were analysed with LIBS. This interval was then used as a guide to map areas of the bedrock not measured by LIBS, with colour and lightness parameters characteristic of magnesium sulfate enrichments. The lithology is also identified from texture, morphology and weathering style in addition to this colour-mapping technique.

Orbital data analysis. The Compact Reconnaissance Imaging Spectrometer for Mars (CRISM) onboard the Mars Reconnaissance Orbiter collects targeted hyperspectral images of the surface with spatial resolution between 12 and 18 m per pixel. Absorption features due to atmospheric carbon dioxide are removed using the Volcano scan method[52]. The discrete ordinate radiative transfer model[53] is used to account for effects due to temporally and spatially variable atmospheric dust and ice aerosols. The observations shown in Supplementary Fig. 11 are map-projected and spectrally smoothed using an iterative log likelihood algorithm to incorporate the instrument's spatial and spectral transfer functions, to retrieve the best estimate of the surface albedo in the presence of Poisson-distributed noise and spatial blur[54]. A Spectral absorption at 1.9 μm is indicative of H_2O within a hydrated mineral, and convexity at 2.29 μm measures the dual presence of the broad hydration absorption and the S-O bending or mineral H_2O overtone commonly observed in hydrated sulfates[55]. Spectra are extracted from spatial regions of interest as determined

by the spatial parameterization, and spectral features are compared to those of laboratory standards to confirm mineral identifications.

Mapping of vein distribution. The presence of veins was mapped along the traverse using MastCam end-of-drive imaging of the surface in front of the rover. The area covered by the images is divided typically into four areas covering ~4 m² of Martian surface. In each area covering bedrock, the presence of veins is reported in vertical and horizontal categories depending on their apparent orientation being either close to vertical or horizontal. In addition, reference cases of dense vein networks are used to report qualitatively the presence of higher density for veins either vertical or horizontal (Supplementary Fig. 12).

Data availability

All in situ and orbital data used in this study are available in the NASA Planetary Data System (https://pds-geosciences.wustl.edu). Other supplementary data that support the findings of this study are available from the corresponding author on reasonable request.

References

44. Grotzinger, J. P. et al. Mars Science Laboratory mission and science investigation. *Space Sci. Rev.* **170**, 5–56 (2012).
45. Mitrofanov, I. et al. Studying of water consent in Mars' gale crater: the first results of the DAN experiment on the NASA curiosity rover. *Dokl. Phys.* **59**, 126–128 (2014).
46. Maurice, S. et al. The ChemCam instrument suite on the Mars Science Laboratory (MSL) rover: science objectives and mast unit description. *Space Sci. Rev.* **170**, 95–166 (2012).
47. Wiens, R. C. et al. The ChemCam instrument suite on the Mars Science Laboratory (MSL) rover: body unit and combined system tests. *Space Sci. Rev.* **170**, 167–227 (2012).
48. Clegg, S. M. et al. Recalibration of the Mars Science Laboratory ChemCam instrument with an expanded geochemical database. *Spectrochim. Acta Part B* **129**, 64–85 (2017).
49. Dyar, M. D. et al. Strategies for Mars remote laser-induced breakdown spectroscopy analysis of sulfur in geological samples. *Spectrochim. Acta Part B* **66**, 39–56 (2011).
50. Schröder, S., Pavlov, S. G., Rauschenbach, I., Jessberger, E. K. & Hübers, H.-W. Detection and identification of salts and frozen salt solutions combining laser-induced breakdown spectroscopy and multivariate analysis methods: a study for future Martian exploration. *Icarus* **223**, 61–73 (2013).
51. Sobron, P., Wang, A. & Sobron, F. Extraction of compositional and hydration information of sulfates from laser-induced plasma spectra recorded under Mars atmospheric conditions—implications for ChemCam investigations on Curiosity rover. *Spectrochim. Acta Part B* **68**, 1–16 (2012).
52. McGuire, P. C. et al. An improvement to the volcano-scan algorithm for atmospheric correction of CRISM and OMEGA spectral data. *Planet. Space Sci.* **57**, 809–815 (2009).
53. Stamnes, K., Tsay, S., Wiscombe, W. & Jayaweera, K. Numerically stable algorithm for discrete-ordinate-method radiative transfer in multiple scattering and emitting layered media. *Appl. Opt.* **27**, 2502–2509 (1988).
54. He, L., O'Sullivan, J. A., Politte, D. V., Powell, K. E. & Arvidson, R. E. Quantitative reconstruction and denoising method HyBER for hyperspectral image data and its application to CRISM. *IEEE J. STARS* **12**, 1219–1230 (2019).
55. Cloutis, E. A. et al. Detection and discrimination of sulfate minerals using reflectance spectroscopy. *Icarus* **184**, 121–157 (2006).